Electronic Supplementary Information

Hierarchically Porous Closed-pore Hard Carbon as Plateau-dominated High-Performance Anode for Sodium-ion Batteries

Experimental Section:

Synthesis of Hard Carbon: Hard carbons were prepared by microwave-assisted solvothermal pre-treatment followed by the single-step carbonization at 1000°C for two hours (4°C min^{-1}) in an inert argon-flow atmosphere (1 L min^{-1}). Here, 10.269 g of sucrose (Merck, 99.5%) and 1.5 mL of concentrated sulphuric acid (Merck, 95%) were dissolved in 150 mL solution of DI water ($\rho \sim 18$ MΩ cm) and diethylene glycol (Sigma-Aldrich, 99%) in the ratio of 4:1 (%v/v). Then, the clear solution was transferred into three autoclaves of volume 90 mL each and microwaved at 200°C for 0.5 h, using a microwave system (Milestone Flexi WAVE). The obtained hydrochar was washed thoroughly, neutralized to a neutral pH value, and dried at 90°C for 12 h. After that, high-temperature carbonization was done to obtain MSHC hard carbon.

Material Characterization: Field-emission gun-scanning electron microscopy was used for the morphological details (FEG-SEM, ZEISS Sigma 300). To investigate the nanostructure of the sample, high-resolution transmission electron microscopy (HR-TEM, JEOL, JEM-2100) was performed. The intrinsic defects of the sample were characterized using powder X-ray diffraction (PXRD, Bruker-D2 Phaser) instrument with Cu Kα (λ = 1.5418 Å) radiation. Further, the defect structures were analyzed by Raman spectroscopy using Horiba T6400 with a 514.5 nm Ar-Krypton mixed ion gas laser. Besides, the surface chemistry and extrinsic defects of the sample were investigated using X-ray photoelectron spectroscopy (XPS) using a monochromatic Al K$_{\alpha}$ X-Ray Source on PHI 5000 VERSA PROBE III (ULVAC PHI (Physical Electronics), USA) XPS instrument. The porosity information, such as surface area and pore

size distribution, was characterized using the nitrogen adsorption/desorption isotherm on the Autosorb IQ instrument at 77K with an outgassing temperature of 200 °C. In addition, to gain insight into the closed porosity of the sample, the Small Angle X-ray Scattering (SAXS) technique was employed, using a XENOCS SAS instrument using synchrotron radiation as the X-ray source (30 W Cu tube with 50KV, 0.6 mA). The cycled electrodes' ex-situ electron paramagnetic resonance (EPR) measurements were performed on Bruker ELEXSYS 580 EPR spectrometer as a first derivative of the absorption signal in the X-band (9.6 GHz) at room temperature. The microwave power and modulation amplitude were used as 15 mW and 5 G, respectively.

Hard Carbon Anode: A homogeneous slurry was prepared by mixing hard carbon, Super-P black carbon, and polyvinylidene difluoride (PVDF, Sigma-Aldrich) in the mass ratio of 8:1:1, using the mortar and pestle for 1 hr, followed by addition of N-methyl-2-pyrrolidone solvent (NMP, Sigma-Aldrich, 99.5%). The hard carbon electrode was prepared by coating the slurry

onto the Cu foil and dried at 80°C in a vacuum oven for 12 h. After that, the electrode was cut into 15 mm diameter with a mass loading of ~ 2 mg cm^{-2}.

Electrochemical Characterization: The stainless-steel coin cells (CR-2032) were fabricated inside the Ar-filled glovebox (M-Braun, H_2O < 0.5 ppm; O_2 < 0.5 ppm). In half-cell configuration, Na metal (10 mm in diameter) and Glass fiber membrane (GF/C, 19 mm in diameter) from Whatman were used as the counter electrode and as the separator, respectively. 1M $NaPF_6$ (Sigma-Aldrich, 98%) in ethylene carbonate (EC) and diethyl carbonate (DEC) (1:1 % v/v, Sigma Aldrich) served as the electrolyte. All galvanostatic charge-discharge (GCD) profiles and cycling performance at different current rates were tested using the Bio-Logic battery testing instrument in the potential range of 1.5 to 0.005 V. The galvanostatic

intermittent titration technique (GITT) was employed at a 0.1 C rate for 30 min and then relaxed for one hour until the potential reached 5 mV.

Ex-situ electrode preparation: The electrodes were discharged up to a particular potential, such as 0.1 V, 0.005 V, and 0 V at a current rate of 0.1C and disassembled inside the glove box. After that, the electrode materials were scraped and taken inside the EPR tube and sealed for the EPR measurement.
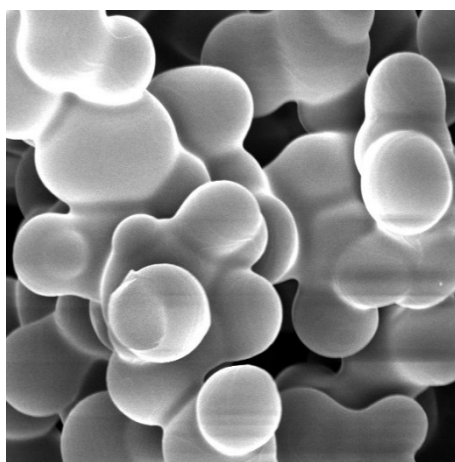

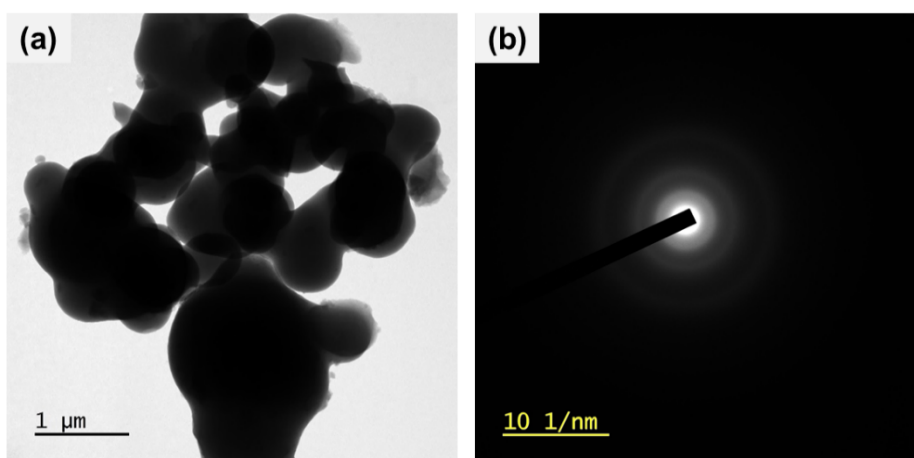**Figure S1**: SEM image of MSHC before heat-treatment carbonization.

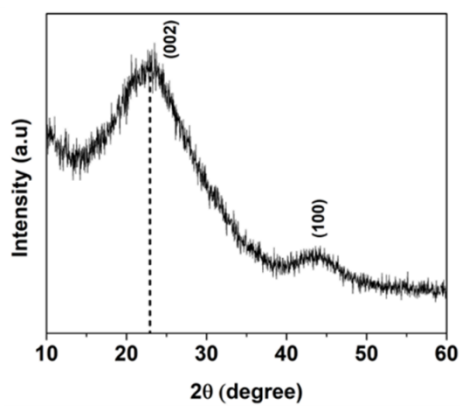**Figure S2**: (a) TEM image, and (b) SAED pattern of MSHC.
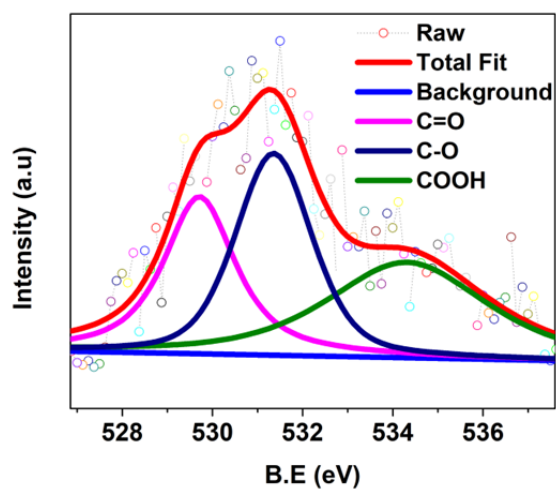
Figure S3: XRD pattern of MSHC.

Figure S4: XPS deconvoluted O1s spectra.

Table S1: Quantitative estimates of oxygen content in the sample

Bonds	Area under curve	Relative proportion in the sample
C=O	2091.548	31.33%
C-O	2460.964	36.87%
(COOH)	2122.49	31.79%

SAXS Data Processing and analysis: The primary data processing, such as scattering vector (or scattering angle) calibration, normalization of the incident beam intensity, and background subtraction, is performed by knowing the incident X-ray wavelength (λ = 1.54 Å) and sample to detector distance (*Chinese Phys. C* **2013**, *37* (10), 108002).

Guinier Analysis: The Guinier formula holds at a small q region to evaluate the size of the particles.[1–3] It is expressed as the following:

$$\ln I(q) = \ln I(0) - (qR_G)^2/3 \qquad\qquad (S1)$$

$$R_G = \sqrt{\frac{3}{5}} \times \frac{D}{2} \qquad\qquad (S2)$$

where I (0) is the scattering intensity at q = 0, R_G is the radius of gyration, and D is the pore's diameter (assumed as spherical in morphology). The figure shows the Guinier plots for MSHC.

Porod Analysis: Porod's law is one of the primary methods in SAXS to quantify the Porod constant and calculate the specific surface area of the sample. Porod's law suggests that the $q^4I(q)$ value will approach a constant K (Porod constant) when q increases to a certain level without any deviation, and it can be expressed as an equation, S3 (*Sci. Rep.* **2017**, *7*, 1–8; *Chem. Mater.* **2022**, *34* (7), 3489–3500):

$$\lim q^4 I(q) = K \qquad \text{or} \qquad \lim \ln[q^4 I(q)] = \ln K \qquad\qquad (S3)$$

where q is the scattering vector, $q = 4\pi \sin \theta/\lambda$, 2θ is the scattering angle, λ is the incident X-ray wavelength, I(q) is the scattering intensity, and K is the Porod constant.

The positive deviation will arise in the Porod plot, suggesting some additional scattering. A correction factor like $\exp(bq^2)$ might be used to rectify the positive divergence, and the Porod constant (K) can be expressed as an equation, S4 (*Sci. Rep.* **2017**, *7*, 1–8; *Chem. Mater.* **2022**, *34* (7), 3489–3500).

$$\ln [q^4 I(q)] = \ln K + bq^2 \qquad (S4)$$

The specific surface area (S) of the samples can be calculated by the following equation (S5):

$$S = \pi P (1-P)K/Q \qquad (S5)$$

where, P is the volume fraction for the porous system, porosity; Q is the invariant, which is

given by $Q = \displaystyle\int_0^\infty q^2 I(q)dq$ \qquad (S6)

(a)

Guinier Plot

(b)

Porod Plot

Porod Constant (ln K)
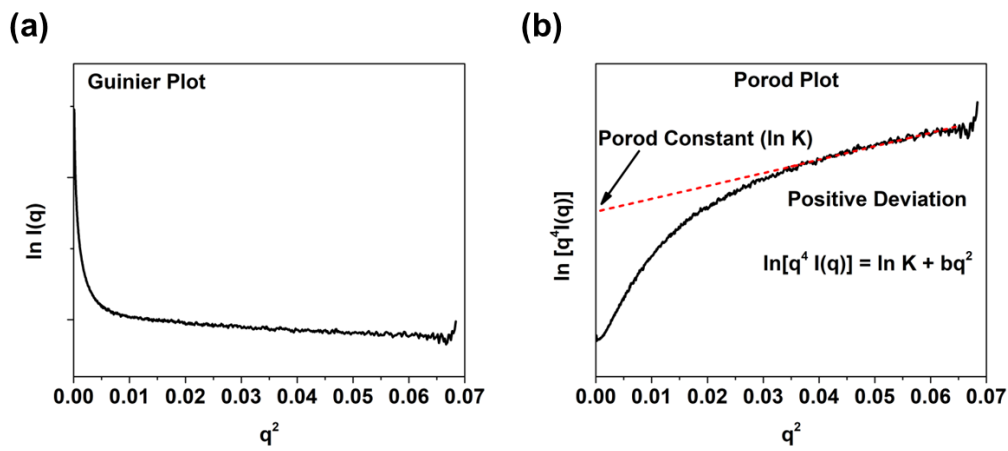
Positive Deviation

$\ln[q^4 I(q)] = \ln K + bq^2$

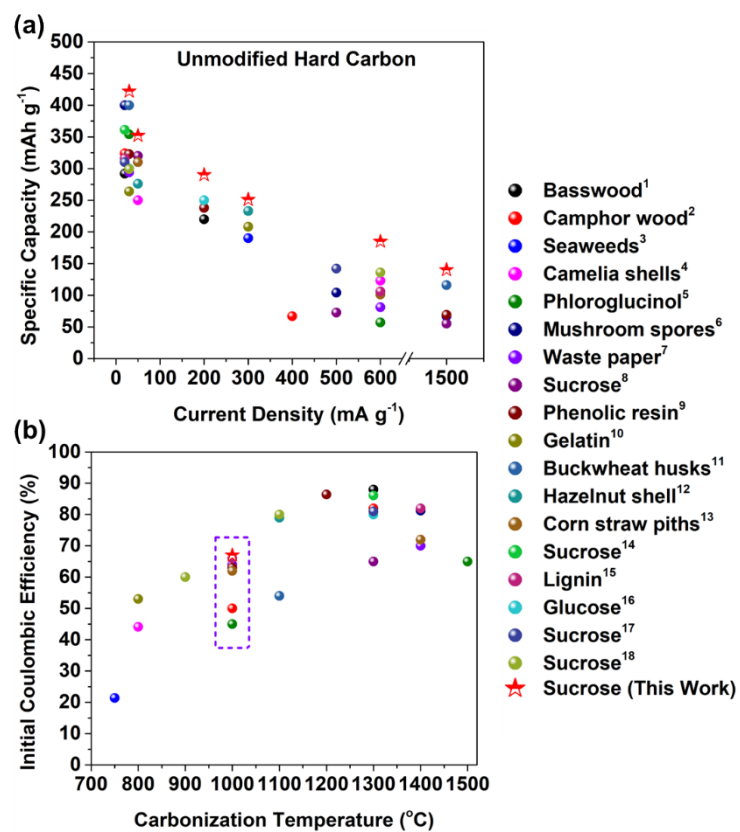**Figure S5:** (a) Guinier plots, and (b) porod plot of MSHC.

Figure S6: Electrochemical performance comparison with the state-of-the-art literature published in the last five years: (a) Specific capacities at different current densities, and (b) initial coulombic efficiency (ICE) at different carbonization temperatures of diverse precursor-based hard carbon anode in SIBs.

Table S2: Comparative electrochemical performance of hard carbon derived from diverse precursor at different carbonization temperature.

S No.	Precursor	Temperature (℃)	Specific capacity	References
1	Basswood	1300	280 mAh g^{-1} @ 30 mA g^{-1} and 215 mAh g^{-1}@ 200 mA g^{-1}	1
2	Camphor wood	1300	325 mAh g^{-1} @ 30 mA g^{-1} and 75 mAh g^{-1}@ 400 mA g^{-1}	2
3	Seaweeds	750	180 mAh g^{-1} @ 300 mA g^{-1}	3
4	Camelia shells	800	250 mAh g^{-1} @ 50 mA g^{-1} and 125 mAh g^{-1}@ 600 mA g^{-1}	4
5	Phloroglucinol	1500	354 mAh g^{-1} @ 30 mA g^{-1} and 57 mAh g^{-1}@ 600 mA g^{-1}	5
6	Mushroom spores	1400	411 mAh g^{-1} @ 20 mA g^{-1} and 104 mAh g^{-1}@ 500 mA g^{-1}	6
7	Waste Paper	1400	319 mAh g^{-1} @ 30 mA g^{-1} and 81 mAh g^{-1}@ 600 mA g^{-1}	7
8	Sucrose	1300	325 mAh g^{-1} @ 50 mA g^{-1} and 70 mAh g^{-1}@ 1500 mA g^{-1}	8
9	Phenolic resin	1200	330 mAh g^{-1} @ 30 mA g^{-1} and 75 mAh g^{-1}@ 1500 mA g^{-1}	9
10	Gelatin	800	264 mAh g^{-1} @ 30 mA g^{-1} and 208 mAh g^{-1}@ 300 mA g^{-1}	10
11	Buckwheat husks	1100	400 mAh g^{-1} @ 50 mA g^{-1} and 116 mAh g^{-1}@ 1500 mA g^{-1}	11
12	Hazelnut shell	1100	276 mAh g^{-1} @ 100 mA g^{-1} and 233 mAh g^{-1}@ 300 mA g^{-1}	12
13	Corn Straw piths	1400	310 mAh g^{-1} @ 50 mA g^{-1} and 101 mAh g^{-1}@ 1000 mA g^{-1}	13
14	Sucrose	1300	361 mAh g^{-1} @ 20 mA g^{-1}	14
15	Lignin	1400	316 mAh g^{-1} @ 30 mA g^{-1} and 106 mAh g^{-1}@ 600 mA g^{-1}	15

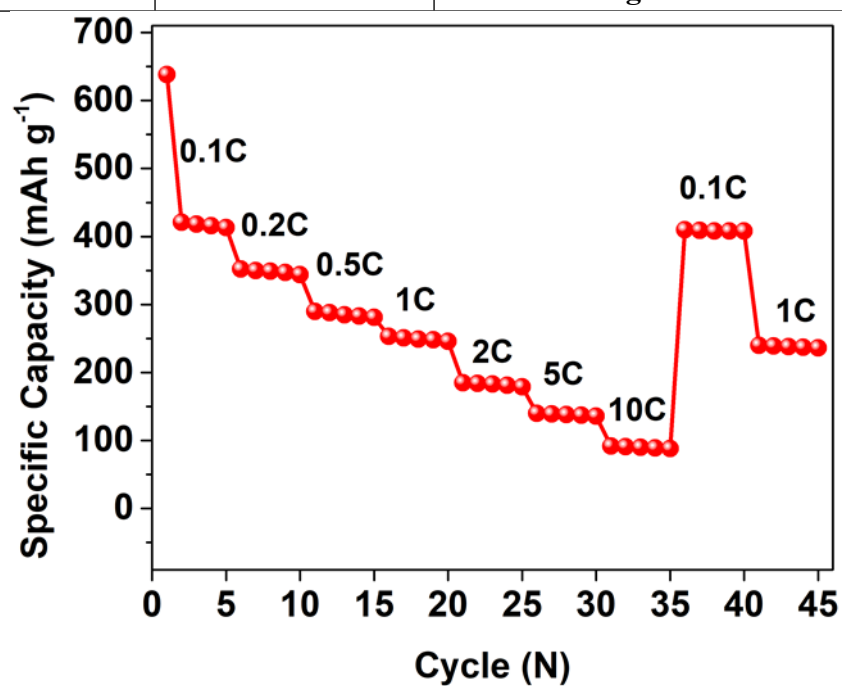| 16	Glucose	1300	360 mAh g^{-1} @ 30 mA g^{-1} and 250 mAh g^{-1}@ 200 mA g^{-1}	16
17	Sucrose	1300	310 mAh g^{-1} @ 30 mA g^{-1} and 160 mAh g^{-1}@ 500 mA g^{-1}	17
18	Sucrose	1100	299 mAh g^{-1} @ 30 mA g^{-1} and 136 mAh g^{-1}@ 5000 mA g^{-1}	18
19	**Sucrose (MSHC)**	**1000**	**422 mAh g^{-1} @ 30 mA g^{-1} and 150 mAh g^{-1}@ 1500 mA g^{-1}**	**This Work**

Figure S7: C-rate performance during discharge of MSHC half-cell
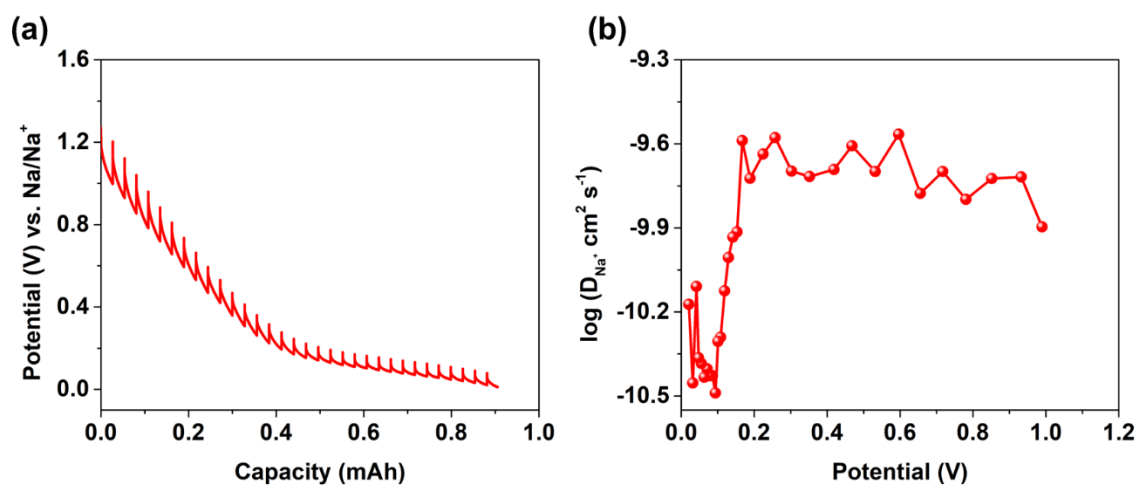
Figure S8: GITT profile at 0.1 C rate, and (f) diffusion coefficient as a function of discharge potential during discharge.
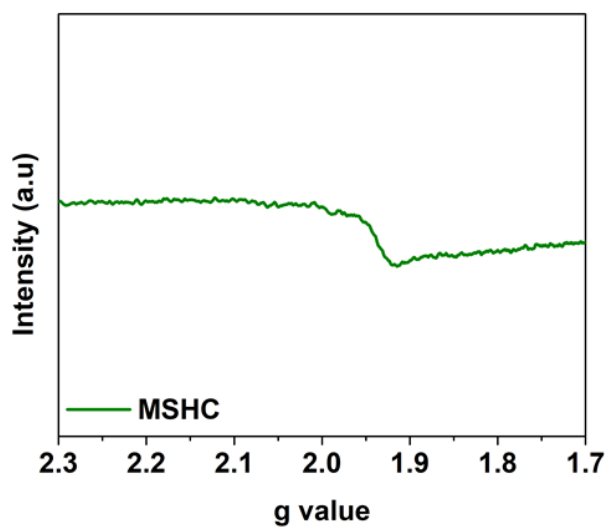

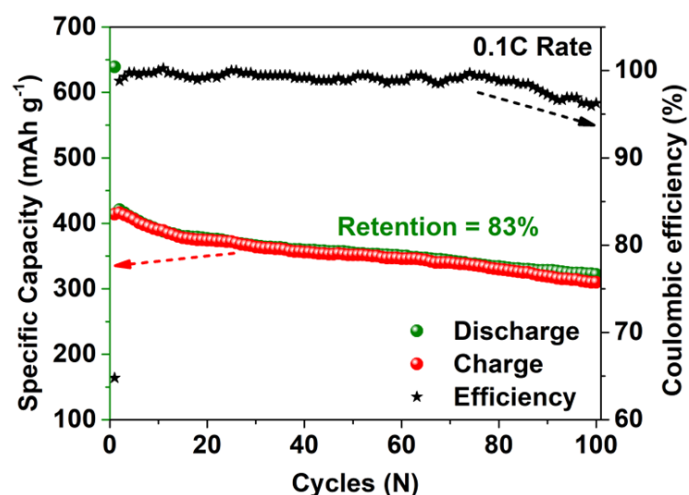**Figure S9**: EPR of hard carbon (MSHC)

Figure S10: Cycling performance of MSHC anode at 0.1C rate for 100 cycles
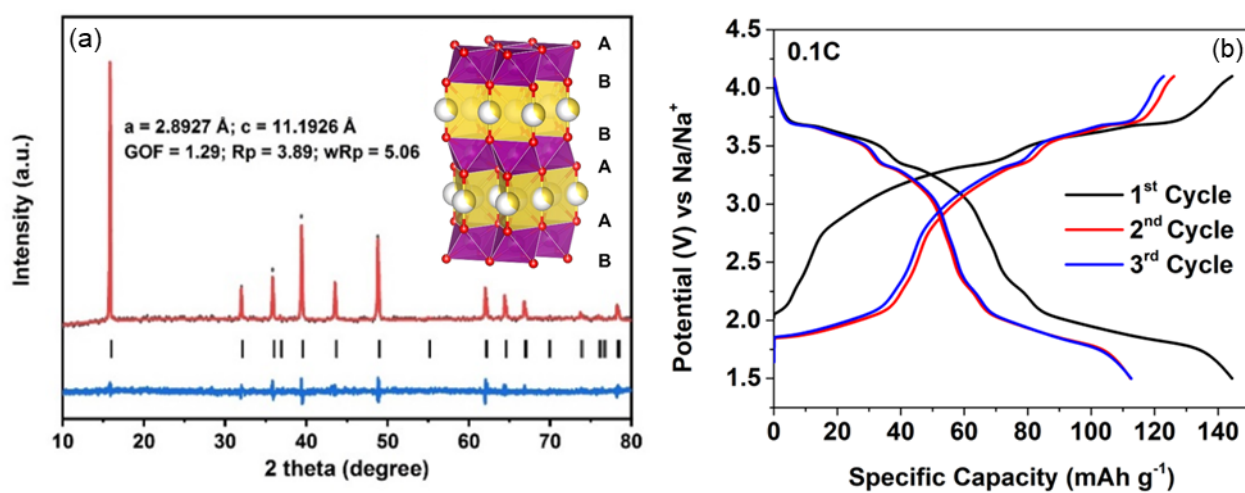

Figure S11: (a) PXRD with refined lattice paramerts and crystal structure of P2-type NNMO cathode (b) Galvanostatic charge-discharge profile of NNMO cathode in half cell configuration at 0.1C rate.

References:

1. Wang, P., Guo, Y. J., Chen, W. P., Duan, H., Ye, H., Yao, H. R., ... & Cao, F. F. (2023). Self-supported hard carbon anode from fungus-treated basswood towards sodium-ion batteries. *Nano Research*, *16*(3), 3832-3838.

2. Guo, S., Chen, Y., Tong, L., Cao, Y., Jiao, H., & Qiu, X. (2022). Biomass hard carbon of high initial coulombic efficiency for sodium-ion batteries: preparation and application. *Electrochimica Acta*, *410*, 140017.

3. Senthil, C., Park, J. W., Shaji, N., Sim, G. S., & Lee, C. W. (2022). Biomass seaweed-derived nitrogen self-doped porous carbon anodes for sodium-ion batteries: Insights into the structure and electrochemical activity. *Journal of Energy Chemistry*, *64*, 286-295.

4. Chen, S., Tang, K., Song, F., Liu, Z., Zhang, N., Lan, S., ... & Wu, Z. (2021). Porous hard carbon spheres derived from biomass for high-performance sodium/potassium-ion batteries. *Nanotechnology*, *33*(5), 055401.

5. Alptekin, H., Au, H., Olsson, E., Cottom, J., Jensen, A. C., Headen, T. F., ... & Titirici, M. M. (2022). Elucidation of the Solid Electrolyte Interphase Formation Mechanism in Micro-Mesoporous Hard-Carbon Anodes. *Advanced materials interfaces*, *9*(8), 2101267.

6. Lyu, T., Liang, L., & Shen, P. K. (2021). Hollow porous carbon spheres for high initial coulombic efficiency and low-potential sodium ion storage. *Journal of Colloid and Interface Science*, *604*, 168-177.

7. Pei, L., Yang, L., Cao, H., Liu, P., Zhao, M., Xu, B., & Guo, J. (2020). Cost-effective and renewable paper derived hard carbon microfibers as superior anode for sodium-ion batteries. *Electrochimica Acta*, *364*, 137313.

8. Xie, H., Wu, Z., Wang, Z., Qin, N., Li, Y., Cao, Y., & Lu, Z. (2020). Solid electrolyte interface stabilization via surface oxygen species functionalization in hard carbon for superior performance sodium-ion batteries. *Journal of Materials Chemistry A*, *8*(7), 3606-3612.

9. Xu, R., Sun, N., Zhou, H., Chang, X., Soomro, R. A., & Xu, B. (2023). Hard carbon anodes derived from phenolic resin/sucrose cross-linking network for high-performance sodium-ion batteries. *Battery Energy*, *2*(2), 20220054.

10. Tong, Y., Wu, Y., Liu, Z., Yin, Y., Sun, Y., & Li, H. (2023). Fabricating multi-porous carbon anode with remarkable initial coulombic efficiency and enhanced rate capability for sodium-ion batteries. *Chinese Chemical Letters*, *34*(1), 107443.

11. Chen, C., Huang, Y., Zhu, Y., Zhang, Z., Guang, Z., Meng, Z., & Liu, P. (2020). Nonignorable influence of oxygen in hard carbon for sodium ion storage. *ACS Sustainable Chemistry & Engineering*, *8*(3), 1497-1506.

12. Moon, H., Innocenti, A., Liu, H., Zhang, H., Weil, M., Zarrabeitia, M., & Passerini, S. (2023). Bio-Waste-Derived Hard Carbon Anodes Through a Sustainable and Cost-Effective Synthesis Process for Sodium-Ion Batteries. *ChemSusChem*, *16*(1), e202201713.

13. Zhu, Y. E., Gu, H., Chen, Y. N., Yang, D., Wei, J., & Zhou, Z. (2018). Hard carbon derived from corn straw piths as anode materials for sodium ion batteries. *Ionics*, *24*, 1075-1081.

14. Xiao, L., Lu, H., Fang, Y., Sushko, M. L., Cao, Y., Ai, X., ... & Liu, J. (2018). Low-defect and low-porosity hard carbon with high coulombic efficiency and high capacity for practical sodium ion battery anode. *Advanced Energy Materials*, *8*(20), 1703238.

15. Zhang, H., Zhang, W., Ming, H., Pang, J., Zhang, H., Cao, G., & Yang, Y. (2018). Design advanced carbon materials from lignin-based interpenetrating polymer networks for high performance sodium-ion batteries. *Chemical Engineering Journal*, *341*, 280-288.

16. Bobyleva, Z. V., Drozhzhin, O. A., Alekseeva, A. M., Dosaev, K. A., Peters, G. S., Lakienko, G. P., ... & Antipov, E. V. (2022). Caramelization as a Key Stage for the Preparation of Monolithic Hard Carbon with Advanced Performance in Sodium-Ion Batteries. *ACS Applied Energy Materials*, *6*(1), 181-190.

17. Zhao, X., Ding, Y., Xu, Q., Yu, X., Liu, Y., & Shen, H. (2019). Low-temperature growth of hard carbon with graphite crystal for sodium-ion storage with high initial coulombic efficiency: a general method. *Advanced Energy Materials*, *9*(10), 1803648.

18. Zhen, Y., Chen, Y., Li, F., Guo, Z., Hong, Z., & Titirici, M. M. (2021). Ultrafast synthesis of hard carbon anodes for sodium-ion batteries. *Proceedings of the National Academy of Sciences*, *118*(42), e2111119118.

19. Pahari, D., Puravankara, S., (2020), On controlling the P2-O2 phase transition by optimal Ti-substitution on Ni-site in P2-type Na0. 67Ni0. 33Mn0. 67O2 (NNMO) cathode for Na-ion batteries, Journal of Power Sources, 455, 227957.